

## MAXIPOL: DATA ANALYSIS AND RESULTS

J. H. P. WU<sup>1</sup>, J. ZUNTZ<sup>2</sup>, M. E. ABROE<sup>3</sup>, P. A. R. ADE<sup>4</sup>, J. BOCK<sup>5</sup>, J. BORRILL<sup>6,7</sup>, J. COLLINS<sup>8</sup>,  
S. HANANY<sup>3</sup>, A. H. JAFFE<sup>2</sup>, B. R. JOHNSON<sup>9</sup>, T. JONES<sup>3</sup>, A. T. LEE<sup>8,10,7</sup>, T. MATSUMURA<sup>3</sup>,  
B. RABII<sup>8</sup>, T. RENBARGER<sup>3</sup>, P. L. RICHARDS<sup>8</sup>, G. F. SMOOT<sup>8,10,7</sup>, R. STOMPOR<sup>11,6</sup>, H. T. TRAN<sup>8,7</sup>,  
C. D. WINANT<sup>8</sup>

*The Astrophysical Journal*, 665:55–66, 2007 August 10

### ABSTRACT

We present results from and the analysis of data from MAXIPOL, a balloon-borne experiment designed to measure the polarization in the Cosmic Microwave Background (CMB). MAXIPOL is the first CMB experiment to obtain results using a rotating half-wave plate as a rapid polarization modulator. We report results from observations of a sky area of 8 deg<sup>2</sup> with 10-arcmin resolution, providing information up to  $\ell \sim 700$ . We use a maximum-likelihood method to estimate maps of the  $Q$  and  $U$  Stokes parameters from the demodulated time streams, and then both Bayesian and frequentist approaches to compute the  $EE$ ,  $EB$ , and  $BB$  power spectra. Detailed formalisms of the analyses are given. We give results for the amplitude of the power spectra assuming different shape functions within the  $\ell$  bins, with and without a prior  $C_\ell^{EB} = C_\ell^{BB} = 0$ , and with and without inclusion of calibration uncertainty. We show results from systematic tests including differencing of maps, analyzing sky areas of different sizes, assessing the influence of leakage from temperature to polarization, and quantifying the Gaussianity of the maps. We find no evidence for systematic errors. The Bayesian analysis gives weak evidence for an  $EE$  signal. The  $EE$  power is  $55^{+51}_{-45} \mu\text{K}^2$  at the 68% confidence level for  $\ell = 151$ –693. Its likelihood function is asymmetric and skewed positive such that with a uniform prior the probability of a positive  $EE$  power is 96%. The powers of  $EB$  and  $BB$  signals at the 68% confidence level are  $18^{+27}_{-34} \mu\text{K}^2$  and  $-31^{+31}_{-19} \mu\text{K}^2$  respectively and thus consistent with zero. The upper limit of the  $BB$ -mode at the 95% confidence level is 9.5  $\mu\text{K}$ . Results from the frequentist approach are in agreement within statistical errors. These results are consistent with the current concordance  $\Lambda\text{CDM}$  model.

*Subject headings:* cosmic microwave background — cosmology: observations — methods: data analysis — polarization

### 1. INTRODUCTION

Observations of the Cosmic Microwave Background (CMB) have dramatically enhanced our understanding of the universe. The recent focus has been on the detection of polarization in the CMB because it provides information complementary to what can be learned from the temperature anisotropy. The discovery and characterization of the polarization not only confirms the cosmological interpretation of the origin of the temperature anisotropy and large-scale structures, but also improves the accuracy with which we measure parameters in our cosmological model, such as the epoch of reionization. So far detection of CMB po-

larization has been reported by DASI (Leitch *et al.* 2005), CBI (Readhead *et al.* 2004; Sievers *et al.* 2005), CAPMAP (Barkats *et al.* 2004), BOOMERANG (Montroy *et al.* 2005), and WMAP (Page *et al.* 2006). Here we report results from MAXIPOL with particular emphasis on the data analysis procedure and cosmological results. A companion paper (Johnson *et al.* 2006) emphasizes the polarimetric instrumentation and observations.

MAXIPOL flew from the NASA Columbia Scientific Ballooning Facility in Ft. Sumner, New Mexico in May 2003. A region of about 8 square degrees, with Galactic coordinates  $l$  between 110.69° and 114.98° and  $b$  between 38.75° and 42.49°, was scanned during a 7.6 hour night scan. This region was located near the star Beta Ursae Minoris ( $\beta$ -UMi). The beam size was 10 arcminutes. We present data collected with 12 polarimeters that have a center frequency of 140 GHz. Polarimetry was implemented by rotating a half-wave plate (HWP) at a frequency of 1.86 Hz and analyzing the modulating polarization with a stationary grid. We refer the reader to the companion paper (Johnson *et al.* 2006) and to other publications for a more thorough review of MAXIPOL and its predecessor MAXIMA (Hanany *et al.* 2000; Lee *et al.* 2001; Stompior *et al.* 2001; Jaffe *et al.* 2001; Wu *et al.* 2001a; Abroe *et al.* 2004).

The characteristics of CMB radiation can be described using the four Stokes parameters: the intensity  $I$ , the linear polarization  $Q$  and  $U$ , and the circular polarization  $V$ . The anisotropy in  $I$  (also called the temperature  $T$ ) has been well measured. The circular component  $V$  can only arise from parity violating physics and is believed to be absent from the

<sup>1</sup> Department of Physics, Institute of Astrophysics, & Center for Theoretical Sciences, National Taiwan University, Taipei 10617, Taiwan

<sup>2</sup> Astrophysics Group, Blackett Lab, Imperial College, London, UK, SW7 2AZ

<sup>3</sup> School of Physics and Astronomy, University of Minnesota, Minneapolis, MN, 55455, USA

<sup>4</sup> School of Physics and Astronomy, Cardiff University, Cardiff, UK, CF24 3YB

<sup>5</sup> Jet Propulsion Laboratory, Pasadena, CA, 91109, USA

<sup>6</sup> Computational Research Division, Lawrence Berkeley National Lab, Berkeley, CA, 94720, USA

<sup>7</sup> Space Sciences Laboratory, University of California, Berkeley, CA, 94720, USA

<sup>8</sup> Department of Physics, University of California, Berkeley, CA, 94720, USA

<sup>9</sup> Astrophysics, University of Oxford, Oxford, UK, OX1 3RH

<sup>10</sup> Physics Division, Lawrence Berkeley National Lab, Berkeley, CA, 94720, USA

<sup>11</sup> Laboratoire AstroParticule et Cosmologie, Université Paris -7, Paris, France

CMB (though this has not been experimentally verified). The  $Q$  and  $U$  parameters arise during the last-scattering process and have been the focus of recent experimental and theoretical work. Their presence is evidence for the standard scenario of the last scattering process and their characteristics carry information complementary to the temperature anisotropy. Alternative to the parameters  $Q$  and  $U$ , one may express the polarization in terms of  $E$  and  $B$ , which are curl and divergence free polarization tensors respectively. For noise-free all-sky data  $Q$  and  $U$  can be converted to and from  $E$  and  $B$  exactly. Otherwise one can only make a statistical conversion between the two. Models of cosmological evolution usually predict the CMB in the form of power spectra: the auto-correlations  $TT$ ,  $EE$ , and  $BB$ , and the cross-correlations  $TE$ ,  $TB$ , and  $EB$ . In this paper we report on measurements of the  $Q$  and  $U$  Stokes parameters, and the corresponding  $EE$ ,  $EB$  and  $BB$  polarization power spectra.

We used two alternative statistical approaches to extract quantities of interest from the data, the Bayesian and frequentist approaches. Both have been used successfully in the analysis of cosmological data. For a given set of data, the Bayesian approach gives the smallest error interval for the estimated quantities, but its application is sometimes computationally intractable.

In our analysis we demodulated the timestreams and subsequently used a Bayesian maximum-likelihood approach to make best-fit maps of the Stokes parameters. We then estimated the  $EE$ ,  $BB$  and  $EB$  polarization power spectra of the CMB using both Bayesian and frequentist approaches. In both cases we accounted for known instrumental effects and conducted tests for systematic errors.

This paper is organized as follows. In Section 2 we describe our analysis formalism and procedures for estimating  $Q$  and  $U$  maps from the time-ordered data (TOD), and power spectra from these maps. In Section 3, we present our results, including the maps, the power spectra, and systematic tests. Our conclusions are given in Section 4.

## 2. FORMALISM FOR DATA PROCESSING

### 2.1. Time-domain processing

The time-ordered data (TOD) were flagged for the presence of transient signals and calibrated using laboratory data and observations of Jupiter. They were cut into segments separated by gaps longer than 30 seconds, depending on both the flagging of transient signals and the stationarity of noise. Various tests were performed to ensure the Gaussianity and stationarity of the noise within each segment (Collins 2006). From each segment we estimated and removed an instrumental signal that was synchronous with the rotation of the HWP, which we call HWP synchronous signal (Johnson 2004), and deconvolved the instrumental filters. See Johnson *et al.* (2006) for more details about these data processing steps.

The TOD of each of the polarimeters can be modelled as

$$d_t = s_t^T + \epsilon \left[ -s_t^Q \cos \phi_t + s_t^U \sin \phi_t \right] + n_t, \quad (1)$$

where

$$\phi_t = 4\beta_t - 2\alpha_t, \quad (2)$$

$d_t \equiv d(t)$ ,  $t$  is time,  $s_t^T \equiv T(\mathbf{x}_t)$ ,  $s_t^Q \equiv Q(\mathbf{x}_t)$ ,  $s_t^U \equiv U(\mathbf{x}_t)$ ,  $n_t$  is the instrumental noise at time  $t$ ,  $\mathbf{x}_t \equiv \mathbf{x}(t)$  is the sky position of the pointing at time  $t$ , and  $\epsilon$  is the modulation efficiency of the polarimeter. The units of  $d_t$  are  $\mu\text{K}$  and thus a calibration factor converting from the measured voltage to tempera-

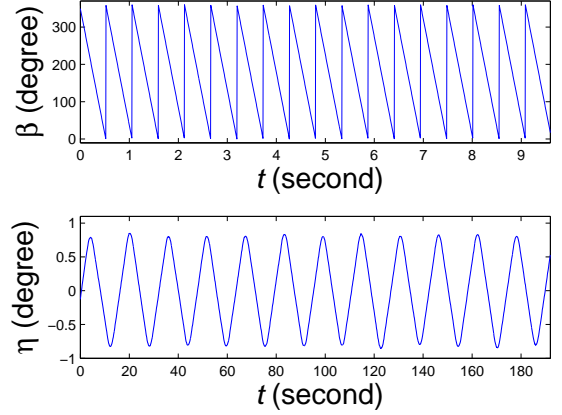


FIG. 1.— HWP rotation angle  $\beta$  (upper panel) and scan angle  $\eta$  (lower panel) from a typical subset of the data.

ture has already been included. We present our results in the WMAP convention with the Stokes parameters  $I$ ,  $Q$ , and  $U$ , taking the North Galactic Pole as the direction of reference for the polarization (Hinshaw *et al.* 2003). The angle  $\alpha_t \equiv \alpha(\mathbf{x}_t)$  is the rotation angle of a vector pointing along a great circle to the zenith, measured relative to the polarization reference vector on the sky. The transmission axis of the polarization analyzer is oriented at 90 degrees to the zenith direction. The angle  $\beta_t \equiv \beta(\mathbf{x}_t)$  is the rotation angle of the HWP relative to the transmission axis of the polarization analyzer. During the observations,  $\alpha_t$  changed at a rate of 15 degrees per hour giving a frequency of  $f_\alpha \approx 1.16 \times 10^{-5}$  Hz while  $\beta_t$  varied at  $f_\beta = 1.86$  Hz. Thus  $f_\phi \approx 4f_\beta = 7.44$  Hz. The temporal data  $d_t$  are sampled at intervals of  $\Delta t = 4.8 \times 10^{-3}$  seconds.

The telescope tracked the guide star  $\beta$ -UMi while scanning in azimuth by 2 degrees peak to peak at a constant frequency  $f_\eta \approx 0.06$  Hz for the majority of the data. Here the subscript  $\eta$  denotes the scan angle. Figure 1 shows typical measurements of  $\beta$  and  $\eta$  from a subset of the data.

To obtain the Time-Ordered Polarization Data (TOPD) we demodulated the TOD to produce independent data streams for  $Q$  and  $U$ . Because of the combination of the HWP rotation and the sky scan, the CMB signal is in side-bands of the fourth harmonic of  $\beta_t$ . Multiplication of the appropriate sinusoid and applying a band-pass filter gives the TOPD from the TOD

$$d_t^Q = \left\langle \frac{-2d_t}{\epsilon} \cos \phi_t \right\rangle, \quad (3)$$

$$d_t^U = \left\langle \frac{2d_t}{\epsilon} \sin \phi_t \right\rangle. \quad (4)$$

The brackets denote a band-pass top-hat filter between 0.05 Hz and 1.5 Hz. This filter selects the frequencies where signals are expected and removes residuals of the HWP synchronous signal, if they exist. Figure 2 shows a power spectrum of a section of the data  $d_t$  before demodulation. The residual peaks (marked by arrows) indicate residuals of subtraction of the HWP synchronous signal. The residuals are at harmonics of  $f_\beta$ . (Figure 6 in the companion paper Johnson *et al.* (2006) shows a similar power spectrum for a different section of the data where the subtraction is more complete.) Figure 3 shows the power spectrum of the data  $d_t$  multiplied by  $-2 \cos \phi_t / \epsilon$ , but before the band-pass filtering; that is, the quantity inside the brackets of equation (3). The gray area indicates the signal band selected by the band-pass

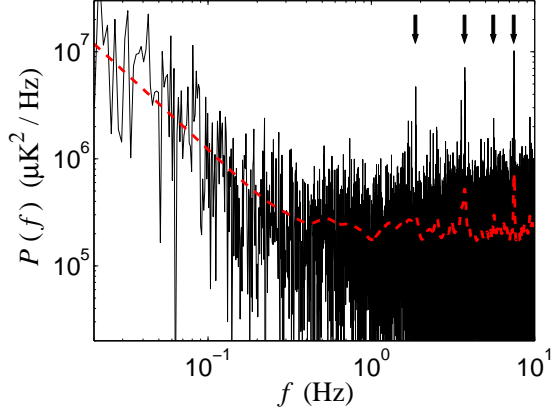


FIG. 2.— Power spectrum for a subset of the TOD  $d_t$ , after removal of the HWP synchronous signal (and after deconvolution of instrumental filters). The solid line is the raw spectrum, and the dashed line is its smoothed estimate. The arrows indicate multiples of the rotation frequency of the HWP  $f_\beta$  showing residuals of the HWP synchronous signal. We give a more complete discussion of this synchronous signal in Johnson *et al.* (2006).

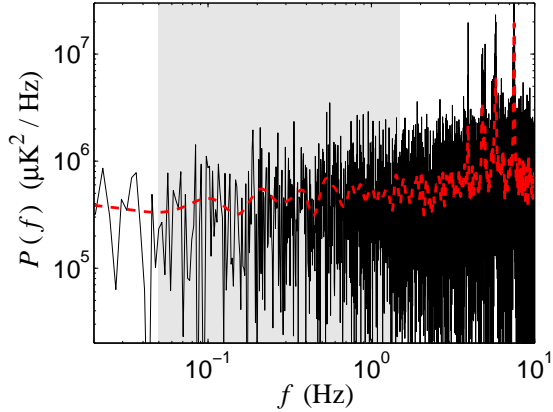


FIG. 3.— Power spectrum of the demodulated  $Q$  of the data in Figure 2 before the band-pass filtering; this is the quantity within the brackets of equation (3). The solid line is the raw spectrum, the dashed line is its smoothed estimate, and the shaded area indicates the pass band of the filter. The spectrum is consistent with white noise within this pass band.

filter. The low side of the band-pass is determined by the scan speed and the high side by the  $\sim 1.3$  Hz cut-off due to the beam. The power spectrum within the band is consistent with white noise and residuals of the HWP synchronous signal are out of band. Simulations with different plausible power spectra for the underlying signal show that the band-pass filtering reduced the RMS of the  $Q$  and  $U$  maps by 4% regardless of the details of the spectra. This loss of signal was compensated for by a Monte-Carlo approach, which we describe later.

Several effects can bias our estimation of the TOPD when using equations (2.1). The beam convolution inevitably removes signal on angular scales smaller than  $\sim 10$  arcminutes. We rectified this by a deconvolution procedure during CMB power spectrum estimation using recipes given in Wu *et al.* (2001b). These recipes also cope with the asymmetry in the beams. This deconvolution is discussed in section 2.3. A second effect is that an imperfect implementation of the demodulation may introduce a bias in the estimation of the CMB signal. For example, the band-pass filtering is equivalent to

a convolution in the time domain so that it induces correlations in the scan direction while giving rise to some loss of signal. A third effect is that the deglitching of the data for the transients creates small gaps in the TOD, and thus may have influenced the demodulation process. The second and third effects were estimated and corrected by a Monte-Carlo approach, as described in section 2.3.

## 2.2. Map making

We employed a standard maximum-likelihood method to obtain maps of  $Q$  and  $U$  from the TOPD. In the time domain the TOPD can be modelled as

$$d_t^X = s_t^X + n_t^X, \quad (5)$$

where  $X = Q$  or  $U$ ,  $s_t^X$  is the CMB signal and  $n_t^X$  is the instrumental noise. We note that  $n_t^Q$  and  $n_t^U$  are independent and thus uncorrelated because the demodulation processes to obtain  $d_t^Q$  and  $d_t^U$  employ orthogonal kernels (see Eqs. (2.1)). We model the CMB signal as

$$s_t^X = A_{tp} s_p^X, \quad (6)$$

and use the Einstein summation convention when appropriate. Here  $A_{tp}$  is the pointing matrix giving the weight of pixel  $p$  in observation  $t$ , and  $s_p^X$  is the CMB signal in the pixel. We took the pointing operator  $A_{tp}$  to be unity when observing pixel  $p$  at time  $t$  and zero otherwise. That is, we assumed the signal  $s_t^X$  to be constant within pixel  $p$ . This model of pixelization induces an extra convolution effect in addition to that from the beam. To deal with these convolution effects we followed the recipes in Wu *et al.* (2001b). These provide a way to transfer all these convolution effects into a single  $B_\ell$  in multipole space, which can then be deconvolved when estimating the CMB power spectrum  $C_\ell$ .

With this modeling, we can estimate the pixelized maps  $m_p^X$  from the temporal data  $d_t^X$ . In the pixel domain we can also model  $m_p^X$  as a linear sum of the signal and the noise components:

$$m_p^X = s_p^X + n_p^X, \quad (7)$$

where  $n_p^X$  is the noise in the pixel domain. Under the assumptions that the noise in the temporal domain is Gaussian and that all CMB maps are a-priori equally likely, the maps  $m_p^X$  can be estimated by maximizing the likelihood of the signal given the data. This gives

$$m_p^X = N_{pp'}^X A_{p't} (N_{t't'}^X)^{-1} d_{t'}^X, \quad (8)$$

where  $A_{p't} = A_{t'p'}^T$ ,  $N_{t't'}^X = \langle n_{t'}^X n_{t'}^{X T} \rangle$  is the time-time noise correlation matrix and  $N_{pp'}^X = \langle n_p^X n_{p'}^{X T} \rangle$  is the estimated pixel-pixel noise correlation matrix given by

$$N_{pp'}^X = [A_{pt} (N_{t't'}^X)^{-1} A_{t'p'}^T]^{-1}. \quad (9)$$

We apply equations (8) and (9) to  $d_t^Q$  and  $d_t^U$  to give the maps  $m_p^Q$  and  $m_p^U$ , respectively, as well as the noise correlation matrices  $N_{pp'}^Q$  and  $N_{pp'}^U$ . The numerical implementation of these equations follows the method described in Stompor *et al.* (2001). We use square pixels that are 3 arcminutes on a side. To simplify notation we construct a column vector

$$m_q = \begin{pmatrix} m_p^Q \\ m_p^U \end{pmatrix}. \quad (10)$$

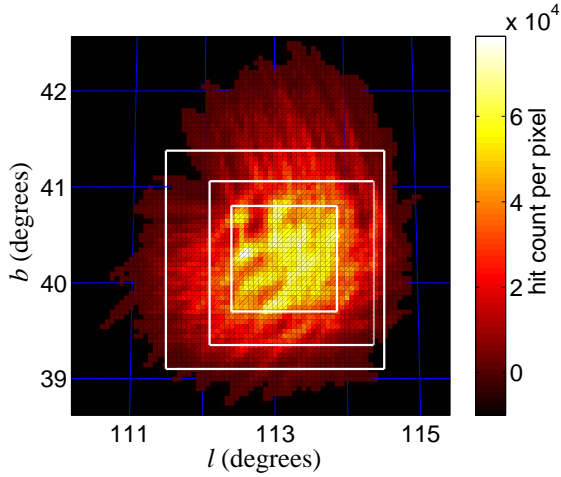


FIG. 4.— The sky coverage of MAXIPOL, presented as the number of 4.8-ms hits per 3-arcminute pixel. The squares are regions of 1.1, 1.7, and 2.3 degrees across, which we use to estimate the power spectra. Pixels with zero hit count but within the square regions have zero weighting in the process of power-spectrum estimation.

Note that we use the subscript  $p$  to denote pixels in the original maps and the subscript  $q$  to denote pixels in the simplified notation. Similarly we write

$$N_{qq'} = \begin{pmatrix} N_{pp'}^Q & \mathbf{0} \\ \mathbf{0} & N_{pp'}^U \end{pmatrix}. \quad (11)$$

Here the off-diagonal blocks are zero in theory because of the orthogonality between  $n_i^Q$  and  $n_i^U$ .

After the maps are formed we apply a filtering to them

$$m_q^W = W_{qq'} m_{q'}, \quad (12)$$

where  $W_{qq'}$  is a filtering matrix. The choice of the filter depends on the subsequent step in the data analysis. For Bayesian power spectrum estimation the maps are left unfiltered (or, equivalently, we apply an identity filter). For the frequentist approach we apply a noise-weighting filter to cope with the anisotropic noise in the pixel domain. Because the hit count per pixel decreases towards the edge of the sky patch, as can be seen in Figure 4, the S/N ratio is higher at the center. To prevent the resulting power spectra from being dominated by the low-S/N pixels, we use

$$W^N = (U^T N^{-1} U)^{-1} U^T N^{-1}, \quad (13)$$

where  $U$  is a column-vector with all entries equal to unity. We also tried other forms of the filter used by other authors (e.g. Montroy *et al.* (2005)), and found that as long as the biasing effect of such filtering is accounted for with the Monte-Carlo process that we will describe later, the final CMB power spectra remain unchanged to a 10% level. For map display purposes we use a Wiener filter

$$W^{\text{WF}} = S(S+N)^{-1}, \quad (14)$$

where  $S \equiv S_{qq'} = \langle s_q s_{q'}^T \rangle$  is the signal-signal correlation matrix. Because the Wiener filter amplifies expected signals in a model-dependent way it induces more bias than other filters that rely purely on the noise level measured from the data. We thus do not use the Wiener filter for power spectrum estimation.

### 2.3. Power-Spectrum Estimation

The  $Q$  and  $U$  can be expanded into spin-2 spherical harmonics in the conventional way:

$$(Q \pm iU)(\mathbf{n}) = \sum_{\ell m} (a_{\ell m}^E \pm i a_{\ell m}^B) \pm 2 Y_{\ell m}(\mathbf{n}), \quad (15)$$

where  $a_{\ell m}^E$  and  $a_{\ell m}^B$  are the coefficients for the  $E$ - and  $B$ -mode polarization, respectively, and  $\mathbf{n}$  is a unit vector directed in the direction of observation. The polarization power spectra can then be defined as

$$C_\ell^{YY'} = \frac{1}{2\ell+1} \sum_m a_{\ell m}^Y a_{\ell m}^{Y'*}, \quad (16)$$

where  $Y$  and  $Y'$  are either  $E$  or  $B$ . To estimate  $C_\ell^{YY'}$ , we use two approaches, one Bayesian and one frequentist, which are described in Sec. 2.3.1 and 2.3.2 respectively. In the following we first lay out the formalism which is general to both approaches.

Because the sky coverage of our observation is finite, we do not probe independent  $C_\ell^{YY'}$  for each multipole  $\ell$ . Instead, we bin the  $\ell$ 's and determine a band power within each  $\ell$  bin. In addition, to increase the signal to noise ratio we use three bins  $\ell = 2-150$ ,  $151-693$ , and  $\geq 694$  such that only the middle bin should have signal given the combination of beam size and sky area.

When estimating the band power and presenting the results we must specify a model for the shape of the power spectrum within each  $\ell$  bin. Given the binned values, we model the power spectra as

$$C_\ell^{YY'} = \mathcal{D}_{\ell\ell'} W_{\ell'b} c_b^{YY'}, \quad (17)$$

where the subscript  $b$  labels an  $\ell$  bin, both  $C_\ell^{YY'}$  and  $c_b^{YY'}$  are treated as column vectors,  $\mathcal{D}_{\ell\ell'}$  is a square diagonal matrix with diagonal elements equal to

$$\mathcal{D}_{\ell\ell} = D_\ell, \quad (18)$$

and  $W_{\ell b}$  is a matrix defined as

$$W_{\ell b} = \begin{cases} 1, & \text{when } \ell \in b, \\ 0, & \text{when } \ell \notin b. \end{cases} \quad (19)$$

Here  $c_b^{YY'}$  is defined as the ‘band power’, and  $D_\ell$  is called the ‘shape function’.

The model for the shape is encoded in  $D_\ell$ . We investigate the following four cases:

$$1. D_\ell^{(1)} = \frac{1}{\ell(\ell+1)}; \quad (20)$$

$$2. D_\ell^{(2)} = C_{\ell(\Lambda\text{CDM})}; \quad (21)$$

$$3. D_\ell^{(3)} = \frac{1}{2\ell+1}; \quad (22)$$

$$4. D_\ell^{(4)} = 1. \quad (23)$$

Here the  $C_{\ell(\Lambda\text{CDM})}$  is the power spectrum predicted by the concordance model of the WMAP+ACBAR+BOOMERanG result in Spergel *et al.* (2006). It is a flat  $\Lambda\text{CDM}$  cosmology with  $\Omega_b h^2 = 0.022$ ,  $\Omega_m h^2 = 0.13$ ,  $h = 0.74$ ,  $\tau = 0.088$ ,  $n_s = 0.95$ , and  $\sigma_8 = 0.74$ . Consequently the power spectra for different models of the shape function are related to the estimated band power as

$$C_{\ell(n)}^{YY'} = \mathcal{D}_{\ell\ell'}^{(n)} W_{\ell'b} c_{b(n)}^{YY'}, \quad (24)$$



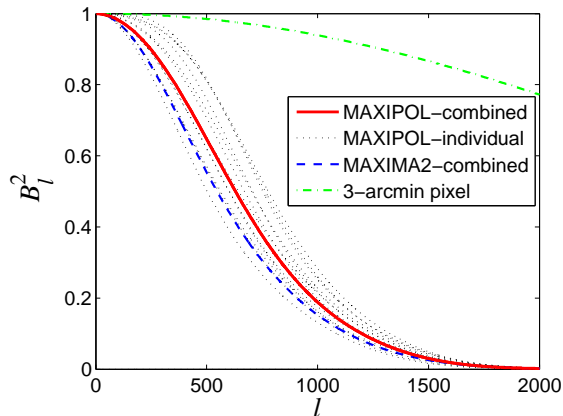


FIG. 5.— The  $B_\ell^2$  function of each of the 12 MAXIPOL polarimeters (dotted), of the noise-weighted combination (solid), of the noise-weighted combination for MAXIMA2 (dashed) (Abroe *et al.* 2004), and of the map pixelization (dot-dashed).

where  $n = 1, 2, 3$ , or 4, and  $c_{b(n)}^{YY'}$  is the band power to be estimated.

Prior to the estimation of the CMB power spectra, we also need to determine the effects of the beam convolution and of the map pixelization, so that these effects can be deconvolved during the estimation process. We follow the recipes described in Wu *et al.* (2001b). The two convolution effects are combined into a single transfer function  $B_\ell$  in the multipole space:

$$B_\ell^2 = B_{\ell(\text{beam})}^2 B_{\ell(\text{pxl})}^2, \quad (25)$$

where  $B_{\ell(\text{beam})}^2$  and  $B_{\ell(\text{pxl})}^2$  are the effective  $B_\ell^2$  of the beam and the pixelization, respectively. The resulting  $B_\ell^2$  for MAXIPOL are presented in Figure 5. The individual  $B_{\ell(\text{beam})}^2$  of the MAXIPOL polarimeters are somewhat smaller than those of MAXIMA and thus produce a wider noise-weighted combination. The figure also shows that with a pixel size of 3 arc-minutes less than 2% of signal power for  $\ell \leq 700$  is attenuated by the pixelization.

### 2.3.1. Bayesian Approach

A commonly used Bayesian approach for power spectrum estimation is the Newton-Raphson algorithm (Bond *et al.* 1998). We attempted to use this method to find the MAXIPOL power spectra, but it failed in a variety of ways that we believe were due to the low signal-to-noise ratio of our maps. The region of parameter space we are exploring is close to the boundary where  $C_\ell = 0$ , and the allowed solutions include negative power values. This region has a non-smooth likelihood that makes the Newton-Raphson method unreliable. We note that future B-mode experiments with a low signal to noise ratio in their B-mode detection are likely to face the same problem. See also Abroe *et al.* (2004) for high signal-to-noise cases where the Newton-Raphson method is also prone to failure. Thus we adopted a Markov Chain Monte-Carlo (MCMC) approach.

The MCMC method explores the likelihood space of the map,  $P(C_\ell|\text{map})$ . It generates lists of samples from a parameter space whose distribution is asymptotically the same as the posterior distribution of the parameters. This approach has a number of advantages: it fully explores the parameter space, making no assumptions about the shape of the likelihood surface, and can be used in any signal-to-noise regime.

The MCMC method is valid in cases where the shape of the posteriors cannot be assumed to take simple forms, such as a Gaussian shape. It also has the important disadvantage of high computational cost.

We used Metropolis-Hastings (MH) sampling, which is one of the simplest forms of MCMC. It has been widely used in cosmological parameter estimation (Spergel *et al.* 2006; MacTavish *et al.* 2005; Lewis and Bridle 2002). This method is also briefly mentioned in Kovac *et al.* (2002). In our case the parameters are binned  $C_\ell$  and the random variable is the map vector,  $m$ , made up of the  $Q$  and  $U$  pixel values. We take the likelihood of the map vector to be Gaussian, with zero mean and inter-pixel covariance matrices  $C = N + S(C_\ell)$ , where  $N$  is the noise covariance and  $S(C_\ell)$  the signal correlation matrix of the proposed  $C_\ell$  (Tegmark and de Oliveira-Costa 2001). Thus the likelihood was calculated exactly using  $\log L = -\frac{1}{2}(m^T C^{-1} m + \text{Tr} \log C)$ . Our MCMC code was derived from the spectrum solver MADspec, which is part of MADCAP (Borrill *et al.* 2006). The computation of the inverse matrix was the largest computational step and was done with a Cholesky decomposition.

To generate sufficient samples for estimating the parameters we used two chains, each of approximately 50,000 samples. The calculation required 24 hours on 128 processors on the Seaborg supercomputer, which belongs to the National Energy Research Scientific Computing Center at Lawrence Berkeley National Laboratory. We are in the process of optimizing the method and believe sufficient computational savings can be made to make the algorithm scalable to somewhat larger datasets.

Posterior likelihoods for binned  $C_\ell$  can easily be calculated with the MH algorithm, since the likelihood of a parameter value is proportional to its multiplicity in the chain. To perform these calculations we used the program GetDist, a part of the CosmoMC package (Lewis and Bridle 2002), which also performs some convergence tests based on derived secondary chains. Additional convergence tests based on power spectra of parameter values in the chain, proposed in Dunkley *et al.* (2005), were also performed. In particular, the variance of the mean of the two chains was less than 10% of the mean of their variances for the parameters of interest.

The choice of a good proposal density is critical to optimize the convergence rate of an MCMC chain. We followed the recommendations in Lewis (2006): We first re-parameterized the space by the eigenvectors of the parameter covariance matrix to mitigate the effect of highly correlated parameters. New proposed jumps were generated along orthonormal basis vectors of this new parameter set which were randomly rotated every  $n_{bin}$  proposals. The length of the jump was a Gaussian random variable with mean zero and the variance of the appropriately rotated eigenvalue multiplied by a scaling factor of 2.4. The covariance matrix was estimated with a short non-optimized MCMC.

### 2.3.2. Frequentist Approach

We also used a frequentist approach to estimate  $C_\ell^{YY'}$ . Frequentist approach was used in the past in analyses of other data sets (Hivon *et al.* 2002; Montroy *et al.* 2005; Page *et al.* 2006; Bond *et al.* 2003). The following sections describe the steps in our analysis and Figure 6 shows a flowchart of the pipeline.

Because the sky patch of our observation is only about 4 degrees across we approximate it as flat to speed up our com-

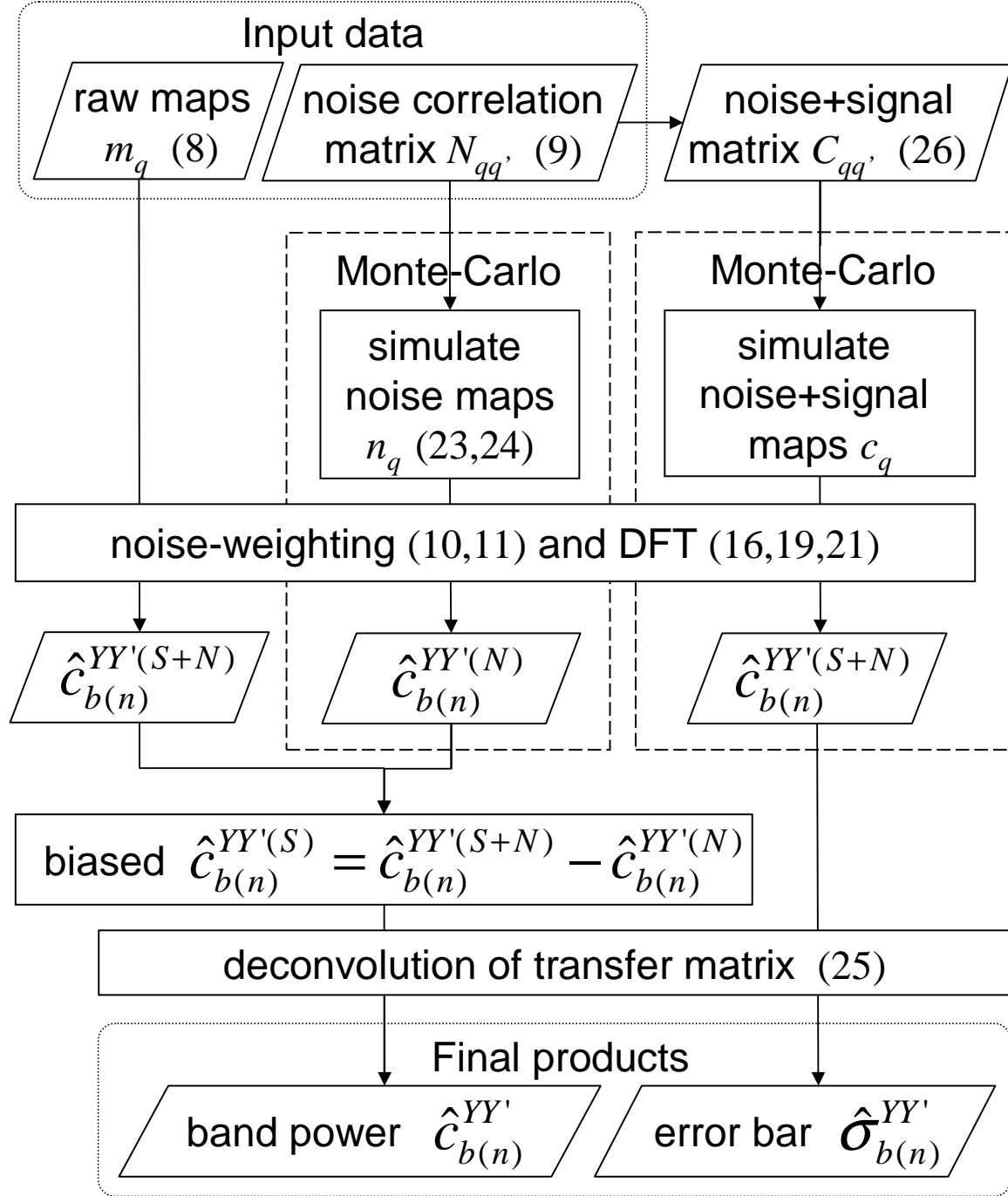


FIG. 6.— Flowchart of the frequentist approach for estimating the CMB power spectra and their associated errors. The numbers in brackets are the equation numbers associated with the operation. The dashed boxes indicate the operations included in the Monte-Carlo simulation.

putation. We use a Discrete Fourier Transform (DFT) to approximate the multipole expansion. With this approximation equation (15) can be reduced and reorganized as

$$\begin{pmatrix} a_{\mathbf{k}}^E \\ a_{\mathbf{k}}^B \end{pmatrix} = \begin{pmatrix} -\cos 2\theta_{\mathbf{k}} & -\sin 2\theta_{\mathbf{k}} \\ \sin 2\theta_{\mathbf{k}} & -\cos 2\theta_{\mathbf{k}} \end{pmatrix} \begin{pmatrix} \tilde{Q}_{\mathbf{k}} \\ \tilde{U}_{\mathbf{k}} \end{pmatrix}, \quad (26)$$

where a tilde denotes the Fourier coefficient of the corresponding quantity,  $\mathbf{k}$  is a Fourier mode, and  $\theta_{\mathbf{k}}$  is the phase angle of  $\mathbf{k}$ . The multipole number can thus be approximated as the wave number,  $\ell \approx k \equiv |\mathbf{k}|$ . As a consequence, equa-

tion (16) reduces to

$$C_{\ell}^{YY'} \approx C_k^{YY'} = \frac{1}{\mathcal{A}} \left\langle \left| a_{\mathbf{k}}^Y a_{\mathbf{k}}^{Y'*} \right|^2 \right\rangle_{|\mathbf{k}|=k}, \quad (27)$$

where  $\mathcal{A}$  is the area of the map used in the DFT in steradians, and the brackets denote an average over all the wave vectors with  $|\mathbf{k}| = k$ .

To increase the S/N ratio per  $\ell$  bin in our results, we combine the  $\ell$ 's into only three bins and estimate their band powers  $c_{b(n)}^{YY'}$ , instead of the  $C_{\ell}^{YY'}$ , with a specified shape function

(see Eqs. (2.3) and (24)). This requires a modification of equation (27) as

$$c_{b(n)}^{YY'} \approx \frac{1}{\mathcal{A}} \left\langle \frac{|a_{\mathbf{k}}^Y a_{\mathbf{k}}^{Y'*}|^2}{D_{\mathbf{k}}^{(n)}} \right\rangle_{|\mathbf{k}| \in b}, \quad (28)$$

where  $D_{\mathbf{k}}^{(n)}$  is the shape function  $D_{\ell}^{(n)}$  convolved by the multipole transform of the sky-coverage window. Note that prior to the DFT, we apply the filtering of equations (12) and (13) to the maps.

Due to the finite sky coverage, the flat-sky approximation, and the filtering of maps, equation (28) is a biased estimator of the band powers. This bias is corrected using the Monte-Carlo approach.

### 2.3.2.1 The Pseudo-Band Powers

We apply the DFT of Equations (26) and (28) to each of the square regions selected from the original maps  $m_p^X$  shown in Figure 4 to obtain the estimated band powers  $\hat{c}_{b(n)}^{YY'(S+N)}$ , where a hat denotes an estimator. We refer to these as the ‘pseudo’-band powers, because they are biased and contain noise. These pseudo-band powers can be modelled as

$$\begin{pmatrix} c_{b(n)}^{EE(S+N)} \\ c_{b(n)}^{BB(S+N)} \\ c_{b(n)}^{EB(S+N)} \end{pmatrix} = H_{\{bb\}\{b'b'\}}^{(n)} \begin{pmatrix} c_{b'(n)}^{EE} \\ c_{b'(n)}^{BB} \end{pmatrix} + \begin{pmatrix} c_{b(n)}^{EE(N)} \\ c_{b(n)}^{BB(N)} \\ c_{b(n)}^{EB(N)} \end{pmatrix}, \quad (29)$$

$$\begin{aligned} c_{b(n)}^{EB(S+N)} &= \left( {}_+H_{bb'}^{(n)} - {}_-H_{bb'}^{(n)} \right) c_{b'(n)}^{EB} \\ &+ c_{b(n)}^{EB(N)}, \end{aligned} \quad (30)$$

where

$$H_{\{bb\}\{b'b'\}}^{(n)} = \begin{pmatrix} {}_+F_{bb'}^{(n)} & {}_-F_{bb'}^{(n)} \\ -{}_F_{bb'}^{(n)} & {}_+F_{bb'}^{(n)} \end{pmatrix} \times \begin{pmatrix} G_{\ell'} B_{\ell'}^2 W_{\ell b'} \\ G_{\ell'} B_{\ell'}^2 W_{\ell b'} \end{pmatrix}, \quad (31)$$

$$\pm H_{bb'}^{(n)} = \pm F_{bb'}^{(n)} G_{\ell'} B_{\ell'}^2 W_{\ell b'}. \quad (32)$$

Here the subscript  $\{bb\}$  denotes the index of  $b$  that runs twice, and similarly for  $\{b'b'\}$ . The  $c_{b(n)}^{YY'}$  are the underlying CMB signals of the field, and the  $c_{b(n)}^{YY'(N)}$  are the noise components of the pseudo-band powers. The  $B_{\ell}$ ,  $G_{\ell'\ell}$ , and  $\pm F_{bb'}^{(n)}$  will be explained as follows.

We call  $B_{\ell}$  the ‘beam transfer function’, which has been discussed earlier. It accounts for the convolution effects from the beam pattern of each of the polarimeters and from the pixelization during the map-making process.

We call the  $G_{\ell'\ell}$  in equations (2.3.2) the ‘time-domain transfer matrix’. It is induced by the time-domain processing, including the effects from the demodulation and the deglitching of the data. Here we use the same  $G_{\ell'\ell}$  for all the  $EE$ ,  $EB$ , and  $BB$  modes because a signal-only Monte-Carlo simulation of 1,000 realizations indicate that it is the same to an accuracy of 2%. This is essentially because the form of  $G_{\ell'\ell}$  is dominated by the band-pass filter in the demodulation process and thus behaves simply as a convolution effect of the sky signal.

We call  $\pm F_{bb'}^{(n)}$  in equations (2.3.2) the ‘DFT transfer matrix’. It accounts for the biasing effect from the DFT approach (Eqs. (12), (13), (26), and (28)). The  ${}_+F_{bb'}^{(n)}$  and  ${}_ -F_{bb'}^{(n)}$  are dominated by the self-coupling and the geometric mixing of E and B polarization respectively (Chon *et al.* 2004).

With the formalism (2.3.2) established, our task becomes to obtain an unbiased estimator of  $c_{b(n)}^{YY'}$ . This requires an inversion of equations (29) and (30). As will be shown, the forms of  $G_{\ell'\ell}$  and  $\pm F_{bb'}^{(n)}$  do not need to be estimated individually. Instead, we estimate the overall transfer matrices  $H_{\{bb\}\{b'b'\}}^{(n)}$  and  $\left( {}_+H_{bb'}^{(n)} - {}_-H_{bb'}^{(n)} \right)$  given a specified shape function  $D_{\ell}^{(n)}$  and the measured  $B_{\ell}$ , and then compute their inverses.

### 2.3.2.2 Estimation of the Noise Component

Following the frequentist approach, we estimate the noise component  $c_{b(n)}^{YY'(N)}$  in equations (2.3.2) by using the previously estimated pixel-pixel noise correlation matrix  $N_{qq'}$  to carry out a Monte-Carlo simulation for the noise-only maps. A Cholesky decomposition gives

$$N_{qq'} = LL^T, \quad (33)$$

where  $L$  is a lower triangular matrix. Then one realization of the simulated noise map is obtained by taking

$$n_q = \begin{pmatrix} n_p^Q \\ n_p^U \end{pmatrix} = Lg, \quad (34)$$

where  $g$  is a vector of Gaussian random numbers with mean zero and variance one. Finally, applying the DFT approach (Eqs. (12), (13), (26), and (28)) to all these noise maps yields an estimated  $\hat{c}_{b(n)}^{YY'(N)}$ . We use 10,000 realizations for the Monte-Carlo to obtain our results.

### 2.3.2.3 Unbiased Estimator

We now construct an unbiased estimator for  $c_{b(n)}^{YY'}$ . Taking the inverse operation of equation (29) gives

$$\begin{pmatrix} \hat{c}_{b(n)}^{EE} \\ \hat{c}_{b(n)}^{BB} \end{pmatrix} = \left( \hat{H}_{\{bb\}\{b'b'\}}^{(n)} \right)^{-1} \times \begin{pmatrix} \hat{c}_{b'(n)}^{EE(S+N)} - \hat{c}_{b'(n)}^{EE(N)} \\ \hat{c}_{b'(n)}^{BB(S+N)} - \hat{c}_{b'(n)}^{BB(N)} \end{pmatrix}, \quad (35)$$

and similarly

$$\begin{aligned} \hat{c}_{b(n)}^{EB} &= \left( {}_+ \hat{H}_{bb'}^{(n)} - {}_- \hat{H}_{bb'}^{(n)} \right)^{-1} \times \\ &\left( \hat{c}_{b'(n)}^{EB(S+N)} - \hat{c}_{b'(n)}^{EB(N)} \right). \end{aligned} \quad (36)$$

The inversion operation for  $\hat{H}_{\{bb\}\{b'b'\}}^{(n)}$  and  $\left( {}_+ \hat{H}_{bb'}^{(n)} - {}_- \hat{H}_{bb'}^{(n)} \right)$  here is feasible only if the underlying matrices are square, i.e., only if the numbers of  $b$ 's and  $b'$ 's are the same. We thus use the same binning strategy for  $b$  and  $b'$  with only three wide bands in obtaining our results.

To estimate  $H_{\{bb\}\{b'b'\}}^{(n)}$ , we employ the following end-to-end Monte-Carlo simulation. We inject a unit power into  $c_{b(n)}^{YY'}$  for one  $\ell$  bin  $b$  at a time. After multiplying the resulting  $C_{\ell(n)}^{YY'}$  obtained from equation (24) with  $B_{\ell(\text{beam})}^2$ , we use

equation (15) to obtain the signal-only high-resolution maps of  $Q$  and  $U$ , which are then scanned and processed to produce mock TOPD. Maps computed from equation (8) using the noise matrices measured from the real data are processed through equations (12), (13), (26), and (28) to yield the resulting band powers. These band powers give one column of the transfer matrix  $H_{\{bb\}\{b'b'\}}^{(n)}$  that corresponds to the chosen  $\ell$  bin for input. A Monte-Carlo simulation with 1,000 realizations is used to obtain each of the six columns in  $H_{\{bb\}\{b'b'\}}^{(n)}$ .

Finally an inversion of  $H_{\{bb\}\{b'b'\}}^{(n)}$  and the previously estimated noise components are used in equations (2.3.2) to yield unbiased estimates of the band powers  $c_{b(n)}^{YY'}$  and thus the power spectra  $C_{\ell(n)}^{YY'}$ .

### 2.3.2.4 Estimation of Error Bars

To estimate the error bars of the power spectra, we again employ a Monte-Carlo simulation. First, we simulate maps that contain both signal and noise using equations (33) and (34), but with the  $N_{qq'}$  replaced by

$$C_{qq'} = S_{qq'} + N_{qq'}. \quad (37)$$

Here  $S_{qq'}$  is the signal-signal correlation matrix based on the  $\hat{c}_{b(n)}^{YY'}$ . The use of the DFT approach and equations (2.3.2) yields the band powers. We compute 10,000 realizations of such band powers, obtain the probability distribution for the power value within each  $\ell$  bin  $b$ , and calculate the 68% confidence intervals.

## 3. RESULTS

### 3.1. Maps and power spectra

Figure 7 shows the maps  $m_p^X$  for the  $Q$  and  $U$  Stokes parameters, the maps convolved with a 10-arcmin Gaussian beam, and the Wiener-filtered maps (see Eqs. (12) and (14)). Note that the three sets have different color ranges. Some uncleaned systematic errors in the TOD, such as long-baseline gain drift, can manifest as non-Gaussian map components, such as scan-stripping or gradients. It is clear that none of the maps show such visible evidence for systematic errors. We will conduct more tests for systematic errors in Section 3.3.

For determining the amplitude of the power spectra we used a square region of 2.3 degrees across centered at  $l = 113^\circ$ ,  $b = 40.25^\circ$  (see Fig. 4) and three  $\ell$  bins:  $\ell = 2-150$ ,  $151-693$ , and  $\geq 694$ . Therefore there are in total nine  $\ell$  bins under consideration, three for each of the  $EE$ ,  $EB$ , and  $BB$  modes. We report results only for the central bin, unless otherwise stated. This is the only bin likely to contain signal, given the beam size and area of the maps. All the Bayesian results are reported after marginalization of the joint posterior likelihood over un-interesting bins. Because there is no tractable Bayesian method to account for the loss of power due to the band-pass filtering during demodulation of the time streams, we rescaled results of  $C_\ell$  for the central  $\ell$  bin by a factor of 1.06, calculated from an appropriate frequentist approach. Bayesian results are quoted as the mode of the likelihood function with 68% intervals of maximum likelihood. Frequentist results are quoted as the median of the probability distribution function with 68% intervals about the median. We used a shape function  $D_\ell^{(1)} = 1/[\ell(\ell+1)]$  unless otherwise noted.

TABLE 1  
AMPLITUDE OF POWER SPECTRA

Shape $D_\ell^{(n)}$	$EE$	$EB$	$BB$
$1/\ell(\ell+1)$	<b>55<sup>+51</sup><sub>-45</sub></b>	<b>18<sup>+27</sup><sub>-34</sub></b>	<b>-31<sup>+31</sup><sub>-19</sub></b>
$\Lambda$ CDM	109 <sup>+130</sup> <sub>-101</sub>	23 <sup>+37</sup> <sub>-37</sub>	-48 <sup>+40</sup> <sub>-25</sub>
$1/(2\ell+1)$	83 <sup>+68</sup> <sub>-50</sub>	24 <sup>+40</sup> <sub>-38</sub>	-51 <sup>+37</sup> <sub>-20</sub>
1	117 <sup>+61</sup> <sub>-77</sub>	32 <sup>+52</sup> <sub>-40</sub>	-41 <sup>+34</sup> <sub>-33</sub>
Bayesian approach (inc. $\sigma_{\text{cal}}$ )			
$1/\ell(\ell+1)$	53 <sup>+57</sup> <sub>-45</sub>	14 <sup>+33</sup> <sub>-31</sub>	-30 <sup>+34</sup> <sub>-21</sub>
$\Lambda$ CDM	113 <sup>+136</sup> <sub>-109</sub>	27 <sup>+36</sup> <sub>-42</sub>	-41 <sup>+39</sup> <sub>-34</sub>
$1/(2\ell+1)$	88 <sup>+70</sup> <sub>-58</sub>	29 <sup>+39</sup> <sub>-45</sub>	-41 <sup>+34</sup> <sub>-31</sub>
1	108 <sup>+80</sup> <sub>-72</sub>	34 <sup>+53</sup> <sub>-46</sub>	-47 <sup>+46</sup> <sub>-29</sub>
Frequentist approach			
$1/\ell(\ell+1)$	62 <sup>+52</sup> <sub>-45</sub>	3 <sup>+33</sup> <sub>-32</sub>	26 <sup>+45</sup> <sub>-50</sub>
$\Lambda$ CDM	68 <sup>+46</sup> <sub>-45</sub>	5 <sup>+34</sup> <sub>-31</sub>	21 <sup>+47</sup> <sub>-38</sub>
$1/(2\ell+1)$	73 <sup>+69</sup> <sub>-43</sub>	23 <sup>+31</sup> <sub>-48</sub>	38 <sup>+42</sup> <sub>-50</sub>
1	72 <sup>+75</sup> <sub>-46</sub>	8 <sup>+46</sup> <sub>-42</sub>	21 <sup>+66</sup> <sub>-58</sub>

NOTE. — Amplitude of power spectra  $\ell(\ell+1)C_\ell^{YY'}/(2\pi)$  in  $\mu\text{K}^2$  for a wide band  $\ell = 151-693$  assuming different shape functions  $D_\ell^{(n)}$ . Errors are 68% confidence intervals. The middle block with '(inc.  $\sigma_{\text{cal}}$ )' gives results including calibration uncertainty  $\sigma_{\text{cal}} = 13\%$ . The first row (bold) is the result for which we show the likelihoods in Figures 8 and 9, and is the result that is shown in Figure 10.

Table 1 gives the amplitude of the polarization power spectra using both analysis methods and for different shape functions  $D_\ell^{(n)}$ . For ease of direct comparison we present all results in  $\ell(\ell+1)C_\ell/(2\pi)$  at the bin center  $\ell = 422$ . The table also gives the results after marginalizing over a calibration uncertainty that is assumed Gaussian with  $\sigma_{\text{cal}} = 13\%$ . The Bayesian and frequentist approaches give consistent results. Results between different shape functions are also consistent within statistical uncertainties.

We note that our Bayesian results are more dependent on shape function than the frequentist results, with a variation approximately one sigma. Such results have been observed by other others, such as in Montroy *et al.* (2005), where the variation is as large as four sigma. In our frequentist results the effect is less apparent, mainly because of the Monte-Carlo bias correction in our pipeline. The origin of this subtle effect warrants further investigation.

Figure 8 gives the Bayesian posterior likelihoods of the  $EE$ ,  $EB$ , and  $BB$  modes. Two of the likelihoods ( $EE$  and  $BB$ ) exhibit a sharp cut-off at the negative end of the parameter axis. The cut-off arises when we marginalize the smooth multi-dimensional likelihood over the eight other parameters (bins). Our likelihood computation method fails (and consequently we have zero samples) when any one eigenvalue of the total covariance matrix becomes negative. Since multiple bins contribute to each eigenmode the cut-offs in the different parameters are coherent, and a sharp edge is formed on marginalization. Because of such correlations between the cut-offs of different parameters, integrating over  $n$  parameters can lead to a cut-off that scales as  $C_\ell^{n-1}$ . Therefore the sharpness reflects the high dimensionality of the marginalized space. It does not bias our analysis.

The posterior likelihood for  $EE$  is skewed positive. By in-



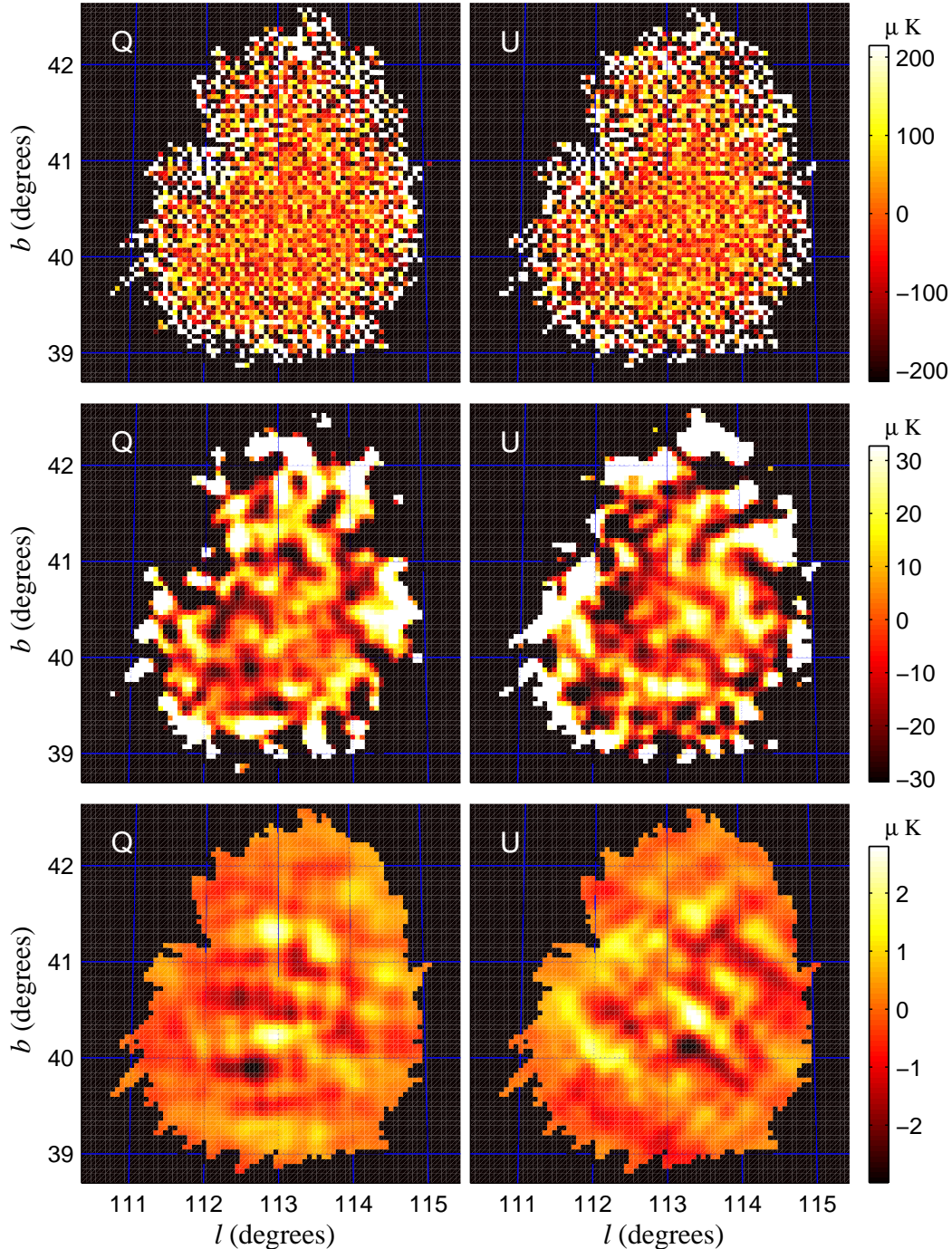


FIG. 7.— The maps of MAXIPOL polarization data (top), the maps convolved with a 10-arcmin Gaussian beam (middle), and the Wiener-filtered maps (bottom).

tegrating the likelihood with a uniform prior over both positive and negative values we found a 96% probability that  $EE$  power is positive. This probability value is unchanged after inclusion of a 13% calibration uncertainty.

The posterior likelihoods for  $EB$  and  $BB$  are consistent with no signal. The 95% confidence intervals for the two modes are  $-53 \mu\text{K}^2 \leq \ell(\ell+1)C_\ell^{EB}/(2\pi) \leq 81 \mu\text{K}^2$  and  $-55 \mu\text{K}^2 \leq \ell(\ell+1)C_\ell^{BB}/(2\pi) \leq 57 \mu\text{K}^2$ , respectively. To obtain an upper limit for the  $BB$ -mode we removed the negative region of its

likelihood (see Fig. 8) and renormalized the rest. We found that at the 95% confidence level  $[\ell(\ell+1)C_\ell^{BB}/(2\pi)]^{1/2} \leq 10.6$  and  $9.5 \mu\text{K}$  with and without the inclusion of calibration uncertainty respectively.

Figure 9 shows Bayesian two-dimensional joint posteriors. Joint distributions that include the  $EE$  mode are skewed positive in  $EE$ . There are sharp cut-offs of the joint likelihood surface for the same reason that they occur in the one-dimensional likelihoods. This results in straight edges for some of the 95% confidence contours.

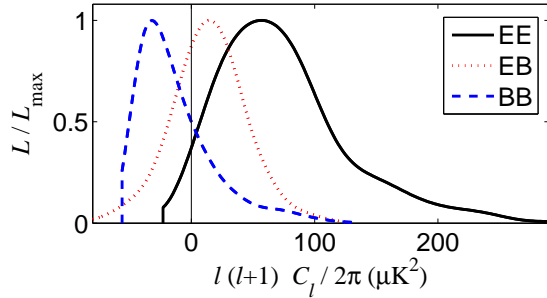


FIG. 8.— One-dimensional marginalized posterior likelihoods of  $\ell(\ell+1)C_\ell^{YY'}/(2\pi)$ . The sharp cut-offs at the negative end reflect the high dimensionality of the marginalized space, and do not bias the analysis (see text).

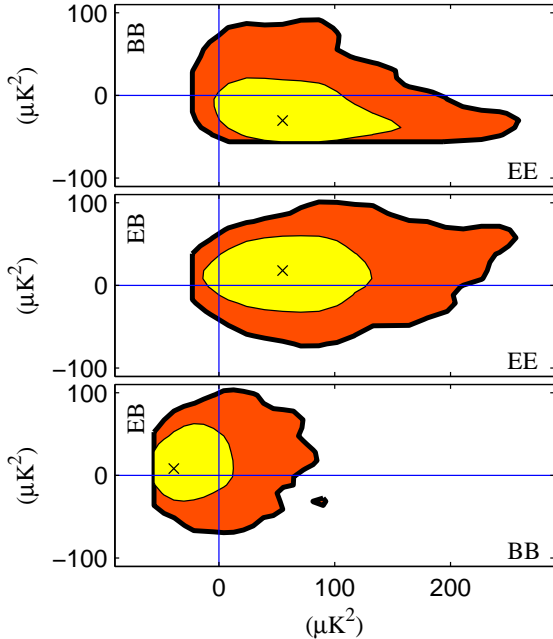


FIG. 9.— Two-dimensional marginalized posterior likelihoods of  $\ell(\ell+1)C_\ell^{YY'}/(2\pi)$ . The inner (thinner) and outer (thicker) contours indicate the confidence regions of 68% and 95% respectively. The crosses mark the locations of maximum likelihood.

We compare the amplitude of the  $EE$  power spectrum with results from other experiments in Figure 10. The right panel in the figure is the same posterior likelihood as shown in Figure 8. Our result is consistent with the prediction of the concordance model, which has a mean value of  $\ell(\ell+1)C_\ell^{EE}/(2\pi) = 14 \mu\text{K}^2$  for our  $\ell$  bin. This value falls at the 65% confidence boundary of our likelihood function around the mode. The lighter shaded region in the right panel of the figure indicates the 68% confidence region of the posterior likelihood. The darker shaded region shows the area under the likelihood where  $EE$  is negative, containing 4% of the total area under the curve.

### 3.2. Significance of the measured power

According to standard cosmological models  $C_\ell^{EB}$  and  $C_\ell^{BB}$  are predicted to be about one order of magnitude smaller than the  $C_\ell^{EE}$  and thus undetected by MAXIPOL. We computed the Bayesian posterior likelihoods for  $\ell(\ell+1)C_\ell^{EE}/(2\pi)$  with a prior  $C_\ell^{EB} = C_\ell^{BB} = 0$ . The results with and without calibra-

TABLE 2  
EE POWER SPECTRUM WITH  $C_\ell^{EB} = C_\ell^{BB} = 0$

Shape $D_\ell^{(n)}$	Mode	68%	95%
Bayesian $C_\ell^{EB} = C_\ell^{BB} = 0$			
$1/[\ell(\ell+1)]$	12	+40 -21	+83 -38
$1/(2\ell+1)$	41	+59 -38	+130 -71
Bayesian $C_\ell^{EB} = C_\ell^{BB} = 0$ (inc. $\sigma_{\text{cal}}$ )			
$1/[\ell(\ell+1)]$	12	+41 -22	+94 -38
$1/(2\ell+1)$	49	+56 -48	+144 -80

NOTE. — Amplitude of power spectrum  $\ell(\ell+1)C_\ell^{EE}/(2\pi)$  in  $\mu\text{K}^2$ , and 68% and 95% confidence intervals assuming different shape functions  $D_\ell^{(n)}$  with a prior  $C_\ell^{EB} = C_\ell^{BB} = 0$ .

TABLE 3  
PROBABILITY FOR  $C_\ell^{EE} > 0$

Shape $D_\ell^{(n)}$	No Prior	$C_\ell^{EB} = C_\ell^{BB} = 0$
$1/[\ell(\ell+1)]$	96%	83%
$\Lambda\text{CDM}$	94%	-
$1/(2\ell+1)$	98%	92%
1	98%	-

NOTE. — Proportion of likelihood with positive  $C_\ell^{EE}$  for different shape functions  $D_\ell^{(n)}$  with no prior, and with a prior  $C_\ell^{EB} = C_\ell^{BB} = 0$  (not all shape functions were considered in this case).

tion uncertainty are summarized in Table 2. A comparison with Table 1 shows that including the priors gives somewhat smaller modes and error bars.

Table 3 summarizes the confidence level at which the hypothesis  $C_\ell^{EE} = 0$  is rejected for different shape functions, and with and without a prior  $C_\ell^{EB} = C_\ell^{BB} = 0$ . The procedure for the calculation is identical to the one already discussed in Section 3.1. We assume a uniform prior for all values of  $EE$  and integrate the area below the appropriate likelihood function on the positive side. Because the posterior likelihoods are all skewed positive most of the confidence levels for a positive  $C_\ell^{EE}$  are above 90%. These numbers do not depend on the magnitude of the calibration uncertainty because the calibration uncertainty is a multiplicative factor, which does not change the fraction of area under the likelihood for values  $C_\ell^{EE} > 0$ .

### 3.3. Systematic error tests

#### 3.3.1. Difference maps

We divided the TOD into two halves in the time domain and processed them separately to yield the CMB maps  $m_q^{(h1)}$  and  $m_q^{(h2)}$ . Separate noise correlation matrices were computed. The difference maps

$$m_q^{(\text{dif})} = m_q^{(h1)} - m_q^{(h2)}, \quad (38)$$

were constructed and the resulting noise matrices computed. We then estimated the polarization power spectra based on these  $Q$  and  $U$  maps, using both Bayesian and frequentist approaches. The rows labeled ‘time’ in Table 4 show the results with and without calibration uncertainty. All these results are consistent with zero.

In a similar manner, we combined half of the 12 polarime-

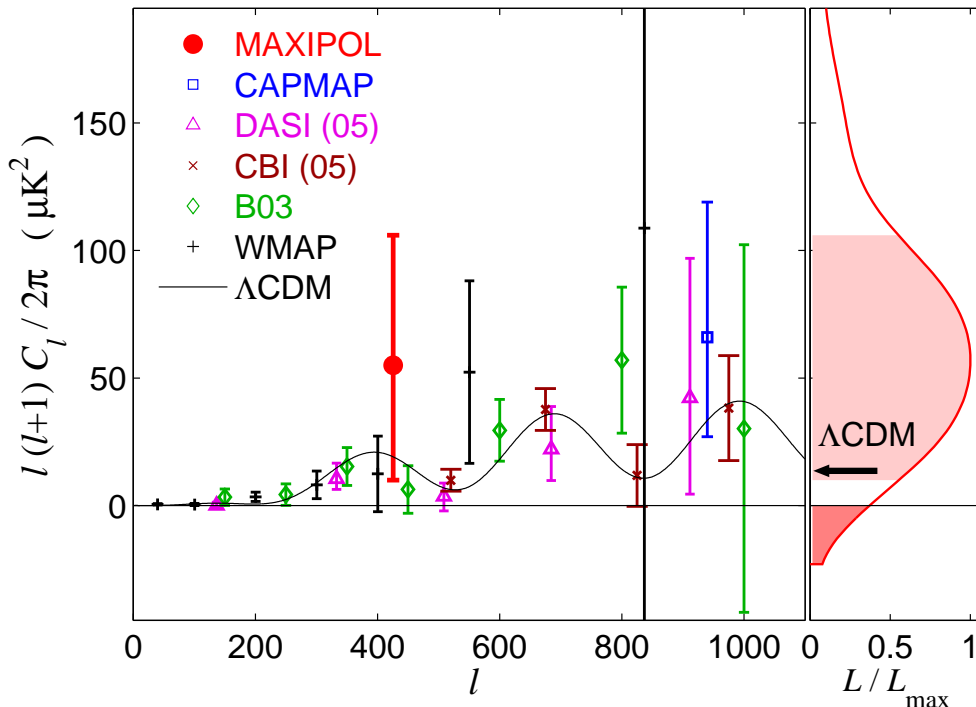


FIG. 10.— The  $\ell(\ell+1)C_\ell^{EE}/(2\pi)$  at  $\ell \leq 1000$  from all experiments which reported CMB polarization. Our result is taken from the first row of Table 1 (numbers in bold type). The other results are from CAPMAP (Barkats *et al.* 2004), DASI (Leitch *et al.* 2005), B03 (Montroy *et al.* 2005), CBI (Sievers *et al.* 2005), and WMAP (Page *et al.* 2006). The right panel is the posterior likelihood of our result. The solid curve in the left panel is a flat  $\Lambda$ CDM model from the WMAP+ACBAR+BOOMERanG result in Spergel *et al.* (2006) (see text for details). It has a mean value of  $\ell(\ell+1)C_\ell^{EE}/(2\pi) = 14 \mu\text{K}^2$  for our bin at  $\ell = 151\text{--}693$  (shown as an arrow in the right panel). The shaded regions in the right panel indicate the 68% confidence region of the posterior likelihood and the region with negative  $EE$  power, which is 4% of the total area below the likelihood curve.

TABLE 4  
POWER SPECTRA OF DIFFERENCE MAPS

Test	Appr.	$EE$	$EB$	$BB$
time	B	$-19^{+54}_{-29}$	$-55^{+33}_{-38}$	$8^{+45}_{-48}$
time	B ( $\sigma_{\text{cal}}$ )	$-10^{+48}_{-39}$	$-55^{+35}_{-42}$	$8^{+49}_{-49}$
time	F	$21^{+48}_{-51}$	$8^{+43}_{-42}$	$-25^{+45}_{-47}$
polar	F	$-5^{+42}_{-41}$	$35^{+41}_{-42}$	$30^{+43}_{-48}$

NOTE. — Amplitude of power spectra  $\ell(\ell+1)C_\ell^{YY'}/(2\pi)$  estimated from difference maps that were constructed with different divisions of the data (column ‘Test’). Division was done either in time or by polarimeter (labeled ‘time’ or ‘polar’ respectively, see text). Results are given both for the Bayesian (B) and frequentist (F) approaches. Error values indicate 68% confidence intervals.

ters to make one set of maps, and the other half for another set, and computed difference maps and the associated noise matrices. The row labeled ‘polar’ in Table 4 shows the results.

Within statistical uncertainties neither the time-domain differencing nor the polarimeter differencing test gives evidence for systematic errors. We note that the sizes of the 68% confidence intervals in Table 4 are on average larger than those of the  $EB$  and  $BB$  modes in Table 1 because the differencing process inevitably increases the noise level per pixel.

### 3.3.2. Regions of different sizes

We also investigated the dependence of the frequentist results on the size of the square patch chosen for the power spectrum estimation. The square regions of different size that we

TABLE 5  
POWER SPECTRA OF DIFFERENT SKY SIZES

Region Size ( $x^\circ \times x^\circ$ )	$EE$	$EB$	$BB$
$x = 1.7$	$69^{+47}_{-48}$	$12^{+52}_{-47}$	$22^{+50}_{-47}$
$x = 1.1$	$63^{+48}_{-44}$	$8^{+50}_{-42}$	$14^{+51}_{-44}$

NOTE. — Amplitude of power spectra  $\ell(\ell+1)C_\ell^{YY'}/(2\pi)$  estimated from square regions of different size (see Fig. 4). The error numbers indicate the 68% confidence intervals.

used are indicated by the boxes in Figure 4. The square region of width  $1.7^\circ$  is centered at  $l = 113.23^\circ$ ,  $b = 40.2^\circ$ . The square region of width  $1.1^\circ$  is centered at  $l = 113.13^\circ$ ,  $b = 40.25^\circ$ . The results are summarized in Table 5 and are consistent with the earlier results. There is no significant increase in the error bars when using a smaller region of the maps because the edges of the square regions are noisier than the central portion (see Fig. 4) and pixels near the edges have negligible statistical weight in the power spectrum estimation.

### 3.3.3. Gaussianity test for the maps

Gaussianity in the pixel-domain signal is an essential assumption for the methods of power spectrum estimation that we used. To test our  $Q$  and  $U$  maps we applied the Kolmogorov test to the eigenvalue-normalized Karhunen-Loeve coefficients, as performed in Wu *et al.* (2001a). If the signal is Gaussian, then the K-L coefficients should be normally distributed. In the process, we found that some of the eigenvalues of the noise-whitened signal matrix were negative owing

to the high noise and imperfectly estimated signal in those modes. We thus excluded these modes from the test, but included all the other modes. These coefficients passed with a clear margin the Kolmogorov test for Gaussianity at 95% confidence.

### 3.3.4. Beam asymmetry and polarization leakage

In certain circumstances an asymmetry in the beam may induce spurious polarization signals. For example, if an asymmetric beam rotates simultaneously with the HWP, the resulting  $EE$  or  $BB$  spectrum will contain power leakage from the  $TT$  mode.

Scans of Jupiter were used to quantify leakage from  $T$  to  $Q$  and  $U$ . Jupiter has an inherent polarization of less than 0.2% at 140 GHz (Clemens *et al.* 1990), which is small compared to the noise on  $Q$  and  $U$  during beam mapping. Out of 12 polarimeters only two showed an instrumental polarization signal at a level of 4% and 5%. No other polarimeter showed leakage from temperature to  $Q$  or  $U$  at a level larger than about 1%, which was the typical noise level for this measurement.

To quantify this effect on the power spectrum we performed an end-to-end simulation. Taking the  $\Lambda$ CDM as the underlying model for  $T$  we conservatively assumed 3% leakage into each of  $Q$  and  $U$ , which is equivalent to 4.2% instrumental polarization, for all 12 polarimeters. The TOD were constructed using the beam patterns as measured in flight. We processed this signal-only TOD to obtain maps and power spectra. A Monte-Carlo simulation showed that out of 1,000 realizations the *largest* contribution of this leakage into the final  $EE$  or  $BB$  spectrum was  $3 \mu\text{K}^2$  for our main bin  $\ell = 151\text{--}693$ ; the mean leakage was smaller. This test demonstrates that the final results were not affected by asymmetries in the measured beam profiles and by the polarization leakage.

## 4. CONCLUSIONS

We discussed the analysis of CMB data that were taken with a HWP polarimeter. Demodulation of the time-domain data based on the rotational position of the HWP gave the  $Q$  and  $U$  data. These data showed a white-noise spectrum at frequencies well below 50 mHz for the majority of the data at a level consistent with detector noise. Most of the data were also Gaussian and stationary. We made  $Q$  and  $U$  maps using a maximum-likelihood technique. The maps were also shown to be Gaussian and there was no visible evidence for systematic errors.

We calculated  $EE$ ,  $EB$ , and  $BB$  power spectra using both Bayesian and frequentist techniques. The Bayesian results

gave weak evidence for  $EE$  power that is consistent with  $\Lambda$ CDM cosmology and with previous results. There was no detectable signal for the  $EB$  and  $BB$  spectra. Results from the frequentist analysis were consistent with the Bayesian ones. We calculated results for different shape functions and with different priors and found that the significance of detection of  $EE$  power was between 83% and 98% with most of the results giving a probability larger than 90%. We gave results with and without marginalization over calibration uncertainty. Inclusion of the calibration uncertainty does not change the significance of detection of  $EE$  power.

We presented results from tests for systematic errors including differencing maps, processing sky regions of different sizes, assessing Gaussianity, investigating beam asymmetry and searching for polarization leakage. None of the tests showed evidence for systematic errors.

MAXIPOL is the first experiment to produce CMB data using a modulating HWP. The techniques we developed to analyze such data should have broad applicability for future CMB experiments that are planning to use similar modulation techniques.

We thank Danny Ball and the other staff members at the NASA National Scientific Ballooning Facility in Ft. Sumner, New Mexico for their outstanding support of the MAXIPOL program. MAXIPOL is supported by NASA Grants NAG5-12718 and NAG5-3941; National Science Council, National Center for Theoretical Science, and Center for Theoretical Sciences, National Taiwan University for J.H.P. Wu; PPARC for A. H. Jaffe and J. Zuntz; a NASA GSRP Fellowship, an NSF IRFP and a PPARC Postdoctoral Fellowship for B.R. Johnson; the Miller Institute at the University of California, Berkeley for H. Tran.

We are grateful for computing support from the Minnesota Supercomputing Institute at the University of Minnesota, from the National Energy Research Scientific Computing Center (NERSC) at the Lawrence Berkeley National Laboratory, which is supported by the Office of Science of the U.S. Department of Energy under Contract No. DE-AC03-76SF00098, and from the National Center for High-Performance Computing, Taiwan. We are grateful for discussions with P. Ferreira and members of his research team. We gratefully acknowledge contributions to the MAXIMA payload by A. Boscaleri, P. de Bernardis, V. Hristov, A.E. Lange, P. Mausekopf, B. Netterfield, and E. Pascale, which were useful for MAXIPOL.

## REFERENCES

- Abroe, M.E., *et al.* 2004, 605, 607  
 Barkats, D., *et al.* 2004, ApJ, 619, L127  
 Bond, J.R., *et al.* 1998, Phys. Rev. D57, 4  
 Bond, J.R., Contaldi, C.R., & Pogosyan, D. 2003, Philosophical Transactions Royal Society of London A, 361, 2435  
 Borrill, J., *et al.* (in preparation)  
 Chon, G., *et al.* 2004, MNRAS, 350, 914  
 Clemens, D.P., *et al.* 1990, PASP, 102, 1064C  
 Collins, J.S. 2006, Ph.D. Thesis, University of California, Berkeley  
 Dunkley, J., *et al.* 2005, MNRAS, 356, 3  
 Eriksen, H.K., *et al.* 2004 ApJS, 155, 2  
 Hanany, S., *et al.* 2000, ApJ, 545, L5  
 Hinshaw, G., *et al.* 2003, ApJS, 148, 63H  
 Hivon, E., *et al.* 2002, ApJ, 567, 2  
 Jaffe, A.H., *et al.* 2001, Phys. Rev. Lett., 86, 3475  
 Johnson, B.R. 2004, Ph.D. Thesis, University of Minnesota  
 Johnson, B., Collins, J., *et al.* 2006, ApJ, in preparation (companion paper)  
 Kovac, J.M., *et al.* 2002, Nature, 420, 772  
 Lee, A.T., *et al.* 2001, ApJ, 561, L1  
 Leitch, E.M., *et al.* 2005, ApJ, 624, 10  
 Lewis, A. and Bridle, S. 2002, Phys. Rev. D, 66, 10  
 Lewis, A. 2006, CosmoMC notes, <http://cosmologist.info/notes/cosmomc.ps.gz>  
 MacTavish, C.J., *et al.* 2005, ApJ(submitted)  
 Montroy, T.E., *et al.* 2005, ApJ, 647, 813  
 Page, L., *et al.* 2006, ApJ(submitted)  
 Readhead, A.C.S., *et al.* 2004, Science, 306, 836  
 Sievers, J.L., *et al.* 2005, submitted to ApJ(astro-ph/0509203)  
 Spergel, D.N., *et al.* 2006, ApJ(submitted)  
 Stompor, R., *et al.* 2001, ApJ, 561, L7  
 Stompor, R., *et al.* 2001, Phys. Rev. D, 65, 22003  
 Tegmark, M. and de Oliveira-Costa, A., 2001, Phys. Rev. D, 64, 6  
 Wandelt, B.D., *et al.* 2004 Phys. Rev. D, 70, 8  
 Wu, J.H.P., *et al.* 2001a, Phys. Rev. Lett., 87, 251303  
 Wu, J.H.P., *et al.* 2001b, ApJS, 132, 1